

# Connections between propulsive efficiency and wake structure via modal decomposition

Morgan R. Jones<sup>1,†</sup>, Eva Kanso<sup>1</sup> and Mitul Luhar<sup>1</sup>

<sup>1</sup>Department of Aerospace and Mechanical Engineering, University of Southern California, Los Angeles, CA 90089, USA

(Received 6 October 2023; revised 13 February 2024; accepted 25 April 2024)

We present experiments on oscillating hydrofoils undergoing combined heaving and pitching motions, paying particular attention to connections between propulsive efficiency and coherent wake features extracted using modal analysis. Time-averaged forces and particle image velocimetry measurements of the flow field downstream of the foil are presented for a Reynolds number of  $Re = 11 \times 10^3$  and Strouhal numbers in the range  $St = 0.16$ – $0.35$ . These conditions produce 2S and 2P wake patterns, as well as a near-momentumless wake structure. A triple decomposition using the optimized dynamic mode decomposition method is employed to identify dominant modal components (or coherent structures) in the wake. These structures can be connected to wake instabilities predicted using spatial stability analyses. Examining the modal components of the wake provides insightful explanations into the transition from drag to thrust production, and conditions that lead to peak propulsive efficiency. In particular, we find modes that correspond to the primary vortex development in the wakes. Other modal components capture elements of bluff body shedding at Strouhal numbers below the optimum for peak propulsive efficiency and characteristics of separation for Strouhal numbers higher than the optimum.

**Key words:** swimming/flying, low-dimensional models

## 1. Introduction

The performance characteristics of swimming and flying animals have long motivated the design of autonomous swimmers with similar kinematics for propulsion and navigation. The energetics of fish propulsion and, in particular, their ability to harvest energy in schools or unsteady flow environments (Beal *et al.* 2006) have also spurred the research

† Email address for correspondence: [morganrj@usc.edu](mailto:morganrj@usc.edu)

and development of novel energy harvesters (McKinney & DeLaurier 1981; Jones *et al.* 1997; Bryant, Mahtani & Garcia 2012). Broadly, these animals rely on oscillating or undulating foils for propulsion.

Characterizing the relationship between foil performance and the downstream wake structure has been a long-standing research area. Pioneering work in this area by Triantafyllou, Triantafyllou & Grosenbaugh (1993) analysed the swimming performance of several different fish and showed that fish operate within a narrow Strouhal number range,  $0.2 < St < 0.35$ , that leads to high propulsive efficiency. The Strouhal number is a kinematic parameter defined as  $St = fA/U_\infty$ , where  $A$  is a characteristic length describing the width of the wake,  $f$  is the frequency of oscillation and  $U_\infty$  is the swimming speed. Laboratory experiments also showed high propulsive efficiencies from oscillating foils operating in this Strouhal number range. Complementary stability analyses showed that oscillating foils produce a jet-like wake that is convectively unstable when excited at frequencies corresponding to Strouhal numbers that yield peak propulsive efficiencies. The spatial stability analysis performed by Triantafyllou *et al.* (1993) used the jet profile of a reverse von Kármán vortex street, where two single (S) vortex cores were shed per half-cycle of oscillation, i.e. a 2S wake pattern. Similar relationships between optimal Strouhal number ranges and instabilities of the jet wake were found by Lewin & Haj-Hariri (2003).

The relationship between wake instability and peak propulsive efficiency was studied further by Moored *et al.* (2012), who used particle image velocimetry (PIV) to visualize wake structures produced by a batoid-inspired oscillating fin. These experiments showed multiple peak efficiencies, with some corresponding to a 2P wake pattern, where two pairs (P) of vortex cores are shed per half-cycle, and others corresponding to a 2S wake. Moored *et al.* (2012) also pursued local stability analyses (i.e. relying on a parallel flow assumption) to show that the time-averaged velocity profile exhibits instabilities when excited at frequencies corresponding to peak propulsive efficiency. This phenomenon was termed ‘wake resonance’, suggesting that when the oscillating foil is tuned to optimally excite the wake, it produces the highest propulsive efficiencies. Moored *et al.* (2012) also examined the vorticity perturbations generated by the most unstable modes in an effort to better understand these instabilities. Follow-on work by Moored *et al.* (2014) showed that the ‘resonant frequencies’ correspond to optimal momentum entrainment, both into and out of the jet region. These findings suggest that there is no single wake structure that corresponds to peak propulsive efficiency (Smits 2019). Further examples of 2P vortex patterns have also been found in wakes produced by eels and dolphins (Tytell & Lauder 2004; Smits 2019).

Recent studies have raised questions regarding the validity of wake resonance theory (Arbie, Ehrenstein & Eloy 2016), noting that although correlations exist between unstable frequencies and peak propulsive efficiency from experiments, it is more difficult to establish a causal link between the two. Arbie *et al.* (2016) considered the stability characteristics of momentumless wakes and noted that these wakes may be stable (even if the thrust-producing jet-like component is unstable). It has also been suggested that, while the wake structure provides insight into propulsive efficiency, it cannot provide a complete explanation (Zhang 2017; Taylor 2018). Other studies (Eloy 2012) suggest that the development of the wake structure is a result of, and not a cause of, high propulsive efficiency. The reverse von Kármán wake from an oscillating foil can be shed in more patterns than just the 2S and 2P wake (see, e.g. Lentink *et al.* 2008; Schnipper, Andersen & Bohr 2009; Andersen *et al.* 2017), and each wake structure has an indirect relationship with propulsive efficiency. For example, Mackowski & Williamson (2015) found from

experiments that wake patterns for a pitching foil, where self-interactions of the vortices occur, do not reflect a net force. Thus, observing the wake structure alone is likely not enough to completely determine the propulsive efficiency (Floryan, Van Buren & Smits 2020).

As an alternative approach, we make use of dynamic mode decomposition (DMD) to identify coherent features (or patterns) in the wakes produced by oscillating foils and link these features to propulsive performance. Dynamic mode decomposition, as first introduced by Schmid (2010), is a technique used to approximate the dynamics of a nonlinear system via the identification of a linear operator that evolves the system to the next state. Dynamic mode decomposition can also be thought of as a data-driven stability analysis because each DMD mode is associated with a specific frequency and growth or decay rate, which provides interpretable physical insight into the spatial structures and their dynamic evolution. In contrast to the stability analysis approach, DMD does not require the mean flow to be locally or globally parallel. In the fields of marine propulsion and energy harvesting, DMD and similar modal decomposition techniques have been used on propeller and turbine wakes to characterize wake instabilities, loading conditions and efficiency (Sarmast *et al.* 2014; Araya, Colonius & Dabiri 2017; Magionesi *et al.* 2018; Strom, Polagye & Brunton 2022).

In this study we use the triple decomposition to identify coherent flow features that contribute to drag and thrust production from PIV measurements for the wake past an oscillating foil. We examine both the vorticity and the Reynolds stresses associated with optimized DMD modes across Strouhal numbers ranging from  $St = 0.16$  to  $St = 0.35$ , and compare the results to time-averaged forces and propulsive efficiencies. We find that the use of DMD enables us to link wake structure with wake stability and propulsive efficiency for oscillating foils.

Our study builds upon the foil configuration described by Floryan *et al.* (2020). We focus on rigid foils and present results primarily in the context of swimming performance. While the use of rigid foils represents a simplification of the fluid–structure interactions pertinent to flapping foil propulsion in nature, our results may provide additional insight into coherent flow features that contribute to drag and thrust. Moreover, the observations presented herein are also relevant to the design of autonomous swimming vehicles (Van Buren, Floryan & Smits 2020) and energy harvesting systems (McKinney & DeLaurier 1981) that use rigid oscillating foils.

## 2. Heave and pitch foil parameters

We consider an oscillating NACA-0012 hydrofoil with chord  $c$  and span  $s$  as illustrated in figure 1. The distance  $b = 0.25c$  denotes the point of rotation from the leading edge. The imposed pitching and heaving kinematics of the foil at the point of rotation are described by  $\theta(t) = \theta_0 \sin(2\pi ft + \phi_p)$  and  $h(t) = h_0 \sin(2\pi ft)$ , respectively, where  $\theta_0$  and  $h_0$  are the respective pitching and heaving amplitudes,  $f$  is the frequency of oscillation and  $\phi_p$  is the phase difference between heaving and pitching oscillations. For the experiments described below, the phase difference was set to  $\pi/2$  ( $90^\circ$ ).

The oscillation frequency can be expressed in dimensionless terms as the Strouhal number,

$$St = \frac{fA_{TE}}{U_\infty}. \quad (2.1)$$

Note that the Strouhal number can also be interpreted as the wake width ( $\sim A_{TE}$ ) normalized by the wavelength ( $\sim U_\infty/f$ ). Another important parameter relative to

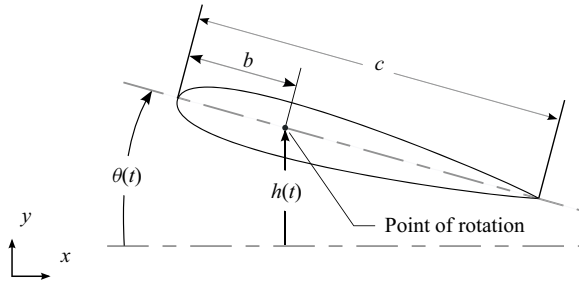


Figure 1. Geometry and parameters for a pitching and heaving hydrofoil.

swimming performance is the angle of attack  $\alpha$ , which is different from the pitch angle due to the influence of the heave velocity,  $\dot{h}(t)$ , and can be expressed as

$$\alpha(t) = \arctan\left(\frac{1}{U_\infty}\dot{h}(t)\right) - \theta(t). \quad (2.2)$$

In the case where the phase angle  $\phi_p$  between pitch and heave is  $90^\circ$ , the maximum angle of attack  $\alpha_0$  can be estimated as

$$\alpha_0 = \arctan\left(\frac{\omega h_0}{U_\infty}\right) - \theta_0, \quad (2.3)$$

where  $\omega = 2\pi f$  is the radian frequency. The time-averaged power and thrust coefficients are described using the following equations:

$$C_P = \frac{\bar{\wp}}{\frac{1}{2}\rho s c U_\infty^3}, \quad C_T = \frac{\bar{\tau}}{\frac{1}{2}\rho s c U_\infty^2}. \quad (2.4a,b)$$

Here  $\rho$  is the density of the fluid,  $\bar{\tau}$  is the time-averaged thrust and  $\bar{\wp} = (1/T)(\int_0^T \dot{h}(t)F_y(t) dt + \int_0^T \dot{\theta}(t)T_z(t) dt)$  is the time-averaged power input to the fluid;  $F_y$  and  $T_z$  are the force and torque associated with the heaving and pitching motions. Propulsive efficiency can then be calculated as

$$\eta = \frac{C_T}{C_P} = \frac{\bar{\tau}U_\infty}{\bar{\wp}}. \quad (2.5)$$

The propulsive efficiency and thrust coefficient are both used to characterize swimming performance. Table 1 shows kinematic parameters and flow conditions examined in the present study. Note that we match kinematic parameters with those from Quinn, Lauder & Smits (2015), who presented a large dataset of propulsive efficiencies for a NACA-0012 foil.

### 3. Experimental methods

Experiments were carried out in a large-scale free-surface water channel with a glass-walled test section of dimensions 7.6 m  $\times$  0.6 m  $\times$  0.9 m. A NACA-0012 hydrofoil with a chord of  $c = 10$  cm and a span of  $s = 32$  cm was used. The foil was three-dimensionally printed from polylactic acid filament, sanded and reinforced with two internal aluminum rods throughout the span. The channel was run at a free-stream speed

Study	Configuration	Type	$Re_c (\times 10^3)$	$St$	$\phi_p$	$\theta_0$	$h^*$
Present study	Pitch and Heave	E	11	0.16–0.59	90°	10°	0.19
Quinn <i>et al.</i> (2015)	Pitch and Heave	E	5–70	0.14–1.4	90°	10°	0.19

Table 1. Parameters used in the present and previous oscillating-foil studies. Chord-based Reynolds number  $Re_c = \rho U_\infty c / \mu$ , Strouhal number,  $St$ , phase between heaving and pitching  $\phi_p$ , pitch amplitude  $\theta_0$  and dimensionless heave ratio  $h^* = h_0/c$ .

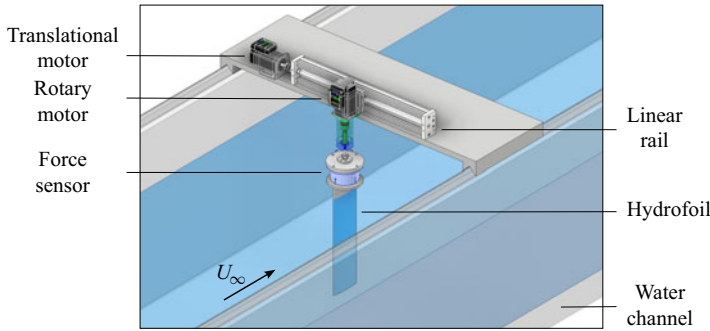


Figure 2. Experimental motion-control system.

of  $U_\infty = 0.1 \text{ m s}^{-1}$  with a turbulence intensity of 1%. Foil motions were produced using a closed-loop control system driven by two NEMA 23 integrated stepper motors, as shown in figure 2. One of the motors was connected to a linear rail to generate the heaving motion. The other motor was mounted to the beam to create the pitching motion. Translational and angular positions of the foil were calculated from the precision micro-steps (3200 steps per revolution) of the stepper motors. Measurements of hydrodynamic forces were made concurrently with an ATI Gamma (SI-32-2.5) six-degree-of-freedom force transducer with a minimum force and torque resolution of 1/80 N and 1/2000 Nm, respectively. Data were acquired at a rate of 5 kHz and filtered using a zero-phase second-order Butterworth filter. Instantaneous forces were measured over oscillation frequencies  $f = 0.4 \text{ Hz} - 1.3 \text{ Hz}$ . For the kinematic parameters used in the present study (table 1), this yielded a Strouhal number range of  $St = 0.16 - 0.59$ . Time-averaged thrust coefficients ( $C_T$ ), power coefficients ( $C_P$ ) and propulsive efficiencies ( $\eta$ ) were computed by combining the force measurements with the foil kinematic data. The standard Klein–McClintock procedure was used to estimate uncertainties for these parameters based on known instrument resolution and measurement uncertainty for the time-averaged thrust and power input (Taylor 1997). Force measurements were collected and averaged for at least 13 periods for each run. Free-stream velocity measurements were recorded using a laser Doppler velocimetry system (MSE miniLDV). Relative uncertainties in the velocity measurements were 0.11%.

Two-dimension two-component (2D-2C) PIV measurements were carried out in the near-wake region of the oscillating foil to provide further insight into the transition from drag-producing and free-swimming conditions to thrust-producing conditions. The PIV system comprised a 5 W 532 nm solid-state laser and a Phantom VEO 410-L high speed camera with  $1280 \times 800$  pixel resolution. Images of the flow field were captured in a field of view of  $27 \text{ cm} \times 17 \text{ cm}$  at a rate of 65 Hz for approximately 56 s. Standard analysis routines in DaVis (LaVision) were used to generate velocity measurements. Two  $64 \text{ pixel} \times 64 \text{ pixel}$  and four  $24 \text{ pixel} \times 24 \text{ pixel}$  convolution windows were used with a

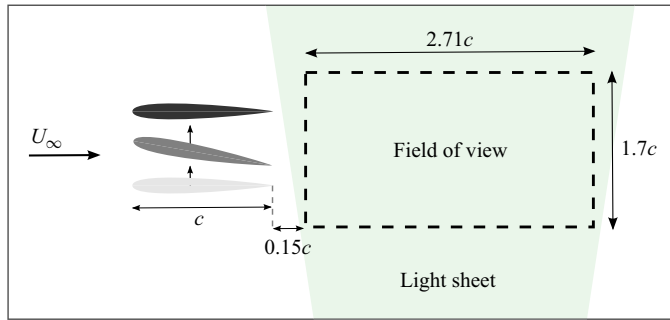


Figure 3. Hydrofoil and PIV experimental set-up with field-of-view dimensions.

50 % overlap to determine the velocity vectors. This yielded a set of  $77 \times 50$  velocity vectors and 3600 snapshots for each of the wakes in this study. Erroneous columns of velocity values from the far ends of the field of view were removed.

Particle image velocimetry flow fields were both phase averaged and time averaged. For the lowest oscillation frequency ( $f = 0.4$  Hz), the available PIV data spanned more than 21 oscillation periods. Dimensions of the field of view relative to the hydrofoil are illustrated in figure 3. Time- and phase-averaged measurements of streamwise velocity and vorticity were computed for the Strouhal numbers  $St = 0.16, 0.23, 0.29$  and  $0.35$ . The respective maximum angles of attack were  $\alpha_0 = 15.2^\circ, 22.3^\circ, 28.2^\circ$  and  $33.1^\circ$ .

### 3.1. Periodic structures via the triple decomposition

For periodic flows under natural or forced conditions, large-scale coherent motions are often present in addition to turbulence. In such situations, the Reynolds decomposition, which assumes that turbulence is the only source of fluctuations in the flow, may not be accurate and can lead to overestimation of the stochastic part of the flow. Alternatively, the full flow field  $\mathbf{u}$  can be expressed as a triple decomposition as introduced by Hussain & Reynolds (1970):

$$\mathbf{u}(\mathbf{x}, t) = \bar{\mathbf{u}}(\mathbf{x}) + \tilde{\mathbf{u}}(\mathbf{x}, \phi(t)) + \mathbf{u}'(\mathbf{x}, t). \quad (3.1)$$

Here  $\bar{\mathbf{u}}$  is the mean (time-averaged) flow field,  $\tilde{\mathbf{u}}$  is the periodic flow field, characterized by the phase parameter  $\phi(t)$ , and  $\mathbf{u}'$  represents the turbulent fluctuations that are incoherent. In our case, where the flow is driven by a known forcing frequency, the periodic component can be directly obtained through phase averaging as

$$\tilde{\mathbf{u}}(\mathbf{x}, \phi_0) + \bar{\mathbf{u}}(\mathbf{x}) = \frac{1}{N} \sum_{n=1}^N \mathbf{u}(\mathbf{x}, \phi_0), \quad (3.2)$$

where the specific phase position  $\phi_0 = \phi(t_0 + n\tau)$  is defined for an initial time  $t_0$  and a period  $\tau$ . However, for natural flows, or those driven by a series of forcing frequencies, (3.2) may be difficult to compute. Instead, phase averaging can be attained through modal decomposition methods. In these cases, the unsteady coherent component  $\tilde{\mathbf{u}}$  may be represented by a linear combination of modes obtained via techniques such as proper orthogonal decomposition (POD) or DMD, and the triple decomposition can be modified

as described by Baj, Bruce & Buxton (2015):

$$\mathbf{u}(\mathbf{x}, t) = \bar{\mathbf{u}}(\mathbf{x}) + \sum_{n=1}^r \tilde{\mathbf{u}}_n(\mathbf{x}, \phi_n(t)) + \mathbf{u}'(\mathbf{x}, t). \quad (3.3)$$

Here,  $r$  is the number of modes retained from the modal decomposition. In this study we use DMD to obtain the periodic component of the flow field in (3.3) and compare this modal representation to the wake characteristics obtained via direct phase averaging, as shown in (3.2).

### 3.2. Dynamic mode decomposition

Dynamic mode decomposition was originally presented to the fluid mechanics community by Schmid (2010) as a method to decompose unsteady or turbulent flow fields into coherent structures. Dynamic mode decomposition can be interpreted as an eigendecomposition of a least squares best-fit linear operator  $\mathbf{A}$  that advances the past snapshots of data (i.e. 2D-2C velocity fields obtained from PIV) forward in time towards future snapshots.

For a set of  $m$  snapshots  $(\mathbf{x}_1, \mathbf{x}_2, \dots, \mathbf{x}_m)$ , the dataset is arranged into two separate matrices of the forms

$$\mathbf{X} = \begin{bmatrix} | & | & \cdots & | \\ \mathbf{x}_1 & \mathbf{x}_2 & \cdots & \mathbf{x}_{m-1} \\ | & | & \cdots & | \end{bmatrix} \quad (3.4)$$

and

$$\mathbf{X}' = \begin{bmatrix} | & | & \cdots & | \\ \mathbf{x}_2 & \mathbf{x}_2 & \cdots & \mathbf{x}_m \\ | & | & \cdots & | \end{bmatrix}, \quad (3.5)$$

with

$$\mathbf{X}' = \mathbf{A}\mathbf{X}. \quad (3.6)$$

Generally,  $\mathbf{A}$  can be approximated by taking the Moore–Penrose pseudo inverse of  $\mathbf{X}'(\mathbf{A} = \mathbf{X}'\mathbf{X}^{-1})$  via the singular value decomposition (SVD):  $\mathbf{X} = \mathbf{U}\mathbf{\Sigma}\mathbf{V}^*$ . However, for high-dimensional datasets such as measurements from PIV snapshots, the computation of  $\mathbf{A}$  is expensive and can be inaccurate due to noisy entries or outliers in the data. To limit computational expense and the impact of noise, we consider the projection of  $\mathbf{A}$  onto a reduced-rank representation of the data obtained via the SVD,  $\mathbf{X} \approx \mathbf{U}_r\mathbf{\Sigma}_r\mathbf{V}_r^*$ , where the subscript denotes a truncation to rank  $r$ :

$$\tilde{\mathbf{A}} = \mathbf{U}_r^*\mathbf{A}\mathbf{U}_r = \mathbf{U}_r^*\mathbf{X}'\mathbf{V}_r\mathbf{\Sigma}_r^{-1}. \quad (3.7)$$

Note that this is analogous to projecting  $\mathbf{A}$  onto the leading POD modes. Subsequently, the eigenvalues of matrix  $\mathbf{A}$  can be estimated by taking the eigendecomposition of  $\tilde{\mathbf{A}}$ ,

$$\tilde{\mathbf{A}}\mathbf{W} = \mathbf{W}\mathbf{\Lambda}, \quad (3.8)$$

where the matrix  $\mathbf{W}$  contains the eigenvectors and  $\mathbf{\Lambda}$  contains the corresponding eigenvalues  $(\lambda_1, \lambda_2, \dots)$ . Dynamic modes for the flow field can be computed using the exact-DMD algorithm from Tu *et al.* (2014) as

$$\mathbf{\Phi} = \mathbf{X}'\mathbf{V}_r\mathbf{\Sigma}_r^{-1}\mathbf{W}_r. \quad (3.9)$$

Here the matrix  $\mathbf{\Phi}$  contains individual dynamic modes  $(\phi_1, \phi_2, \dots)$ . Using this low-dimensional approximation to the dynamics represented by  $\mathbf{A}$ , we can reconstruct the

data using a linear approximation of the dynamic modes for all future times:

$$\mathbf{x}(t) \approx \sum_{k=1}^r \boldsymbol{\phi}_k \exp(\boldsymbol{\omega}_k t) \mathbf{b}_k = \boldsymbol{\Phi} \exp(\boldsymbol{\omega} t) \mathbf{b}. \quad (3.10)$$

The frequency  $\boldsymbol{\omega}_k$  is defined based on the associated eigenvalue  $\lambda_k$  as  $\boldsymbol{\omega}_k = \ln(\lambda_k)/\Delta t$ , where  $\Delta t$  is the time interval between individual snapshots. The vector  $\mathbf{b}$  contains entries of the initial amplitudes  $\mathbf{b}_k$  defined as  $\mathbf{b} = \boldsymbol{\Phi}^{-1} \mathbf{x}_1$ . Recall that the dynamic modes  $\boldsymbol{\phi}_k$  are the columns of the matrix  $\boldsymbol{\Phi}$ . The modes in this temporal DMD formulation represent the absolute stability of the flow field, with the eigenvalues providing insight into oscillation frequencies and growth or decay rates. Given a complex eigenvalue  $\lambda_k = \lambda_{k,r} + i\lambda_{k,i} = |\lambda_k| \exp(i\angle\lambda_k)$ , the frequency can be estimated as  $\boldsymbol{\omega}_k = \boldsymbol{\omega}_{k,r} + i\boldsymbol{\omega}_{k,i} = \ln|\lambda_k|/\Delta t + i(\angle\lambda_k/\Delta t)$ . Thus, a dynamic mode  $\boldsymbol{\phi}_k$  grows over time if the corresponding eigenvalue has amplitude  $|\lambda_k| > 1$  and decays if  $|\lambda_k| < 1$ .

Spatial growth rates can also be approximated by the DMD algorithm by reorganizing the series of snapshots as increasing in space. In this case, modes in spatial DMD represent convective stability, where the eigenvalues would represent spatial frequencies or wavenumbers. In practice, spatial DMD is more prone to noise due to the sparsity of spatial data from PIV measurements, since the number of time snapshots available is typically much higher than the spatial locations (Schmid 2010). For instance, the PIV data obtained in this study span 3600 snapshots in time but only 77 streamwise locations for each run. As a result, we focus on using the temporal DMD approach to take advantage of our time-resolved snapshot data.

### 3.3. Optimized DMD

For the periodic flows that are studied in this paper, it is expected that the dynamic modes should neither grow or decay in time. That is, the eigenvalues of DMD are fixed directly onto the unit circle  $|\lambda_k| = 1$ . However, the presence of even weak noise in periodic flows is known to yield damped eigenvalues,  $|\lambda_k| < 1$ , that result in decay of the corresponding modes ( $\boldsymbol{\phi}_k$ ) over time (Bagheri 2014). Thus, several recent methods have been proposed for debiasing the DMD algorithm in the presence of noisy data, such as measurements from PIV (Dawson *et al.* 2016; Hemati *et al.* 2017; Askham & Kutz 2018). For this purpose, we use the optimized-DMD (opt-DMD) algorithm presented by Askham & Kutz (2018). This is a variant of DMD that uses a variable projection method to approximate the linear operator  $\mathbf{A}$  with reduced noise. Specifically, opt-DMD solves the nonlinear least squares problem

$$\min_{\Lambda, \mathbf{b}} \|\mathbf{X}^T - \boldsymbol{\Phi}(\Lambda)\mathbf{b}\|_F, \quad (3.11)$$

where the eigenvalues in  $\Lambda$  act as iterative parameters and determine the values of the eigenfunctions,  $\boldsymbol{\Phi}$ , and amplitude coefficients,  $\mathbf{b}$ . The algorithm also has the advantage of projecting the modes onto the full dataset rather than a subset from an  $r$ -rank truncation. Additional constraints can be applied to the modes, such as restricting eigenvalues to stay on the unit circle. For simplicity, we do not use any constraints for the flow fields in this study, and find that opt-DMD naturally converges towards the expected eigenvalues in a periodic flow. The DMD modes of velocity are computed using both opt-DMD and exact-DMD algorithms for comparison. We compute the vorticity directly from the opt-DMD modes of velocity to understand the differences between the modal representation and the full flow field.

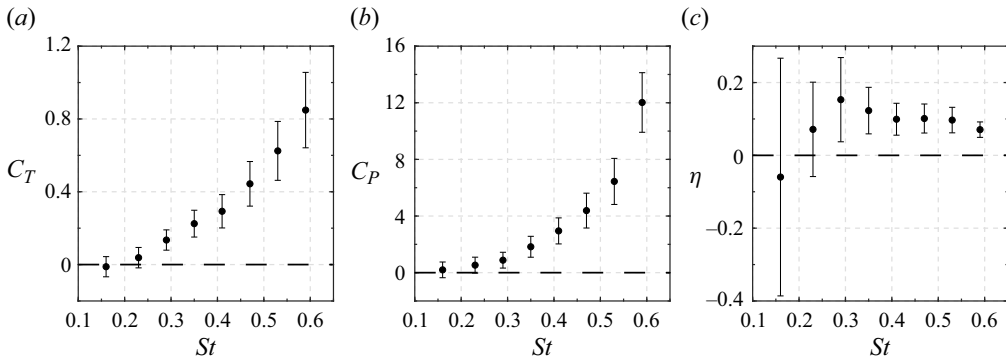


Figure 4. Comparison of time-averaged thrust coefficients and propulsive efficiencies as a function of Strouhal number.

## 4. Results

### 4.1. Propulsive efficiency

Measurements of the thrust coefficient and propulsive efficiency are presented in [figure 4](#). The thrust and power coefficients increase monotonically with increasing Strouhal number. However,  $C_P$  increases faster than  $C_T$  at higher  $St$  values, leading to non-monotonic behaviour in propulsive efficiency and reduced efficiency for  $St > 0.35$ . Peak propulsive efficiencies can be seen within the range of  $0.23 < St < 0.35$ . With the provided uncertainty estimates, it can be argued that either of the three Strouhal numbers  $St = 0.23$ ,  $0.29$  and  $0.35$  result in the highest propulsive efficiency. However, simplified scaling laws suggest that, for angles of attack  $\alpha$  where the flow remains attached to the foil, peak propulsive efficiency can be estimated as

$$St_{max} \approx \sqrt{3}St_0, \quad (4.1)$$

where  $St_0$  is the Strouhal number that results in zero net thrust (Taylor 2018). In our case, the thrust coefficient is near zero for  $St = 0.16$ . Using this value for  $St_0$  gives a maximum efficiency of  $St_{max} \approx 0.28$ . This approximation is consistent with our case of  $St = 0.29$  for which the measured  $\eta$  is highest. Note that the uncertainty in measured efficiency at  $St = 0.16$  is large, which is due to the fact that the thrust and power coefficients are close to 0 for this condition. Nonetheless, this case is similar to a self-propelled swimming mode, where the thrust from the foil is approximately equal to its drag. Negative efficiencies are expected for lower Strouhal numbers,  $St < 0.16$ , for which the net thrust becomes negative due to the effects of viscous drag. As the foil oscillates at lower frequencies, the drag contribution on the propulsor stays approximately constant while the thrust generated decreases (Floryan *et al.* 2017). The present measurements are broadly consistent with trends observed from previous studies (Triantafyllou *et al.* 1993; Quinn *et al.* 2015).

### 4.2. Mean and phase-averaged flow fields

Particle image velocimetry measurements were used to study the downstream wake of the foil for a subset of the Strouhal numbers for which the force measurements were obtained. Phase-averaged vorticity ( $\Omega$ ) and time-averaged streamwise velocity ( $\bar{u}$ ) fields are shown in [figure 5](#), where the foil is positioned to move in the positive  $y$  direction. An increase in magnitude of the jet wake (i.e.  $\bar{u}/U_\infty > 1$ ) can be seen with increasing  $St$ . A near-momentumless wake is observed for  $St = 0.16$ , where the wake profiles are

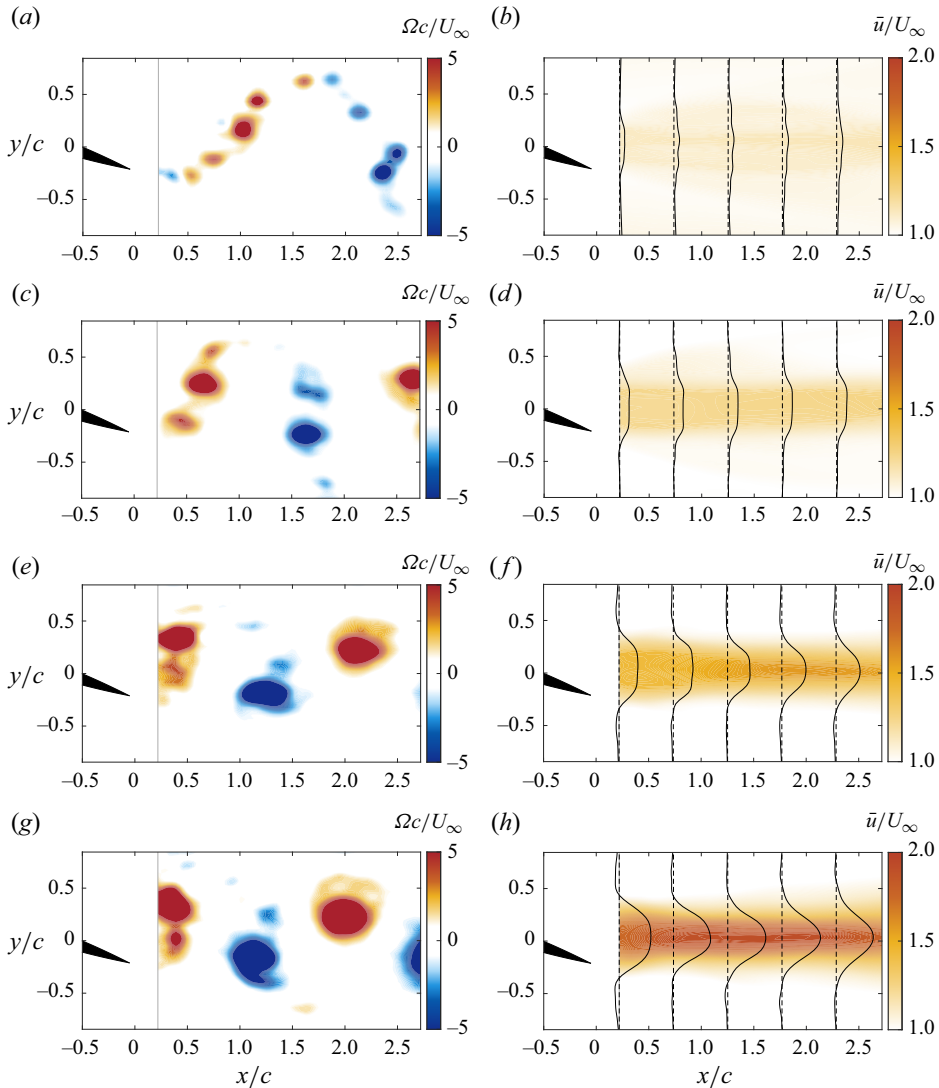


Figure 5. Phase-averaged vorticity and time-averaged streamwise velocity fields for (a,b)  $St = 0.16$ , (c,d)  $St = 0.23$ , (e,f)  $St = 0.29$  and (g,h)  $St = 0.35$ . See also supplementary movie 1 available at <https://doi.org/10.1017/jfm.2024.446>.

close to zero, again indicating a resemblance to self-propelled swimming (figure 5b). Under this condition, approximately five positive and six negative vortices are shed per cycle of oscillation, signifying a small wake asymmetry. The vortices deflect laterally away from the heave and pitch centreline, resulting in an increase of the wake width from  $x/c \approx 0.5$ – $1.5$  that can be seen in figure 5(b).

Increasing the Strouhal number to  $St = 0.23$  produces a 2P wake (figure 5c), with mean profiles that are approximately trapezoidal shaped, with two small but distinct peaks. This wake characteristic matches well with the 2P structure observed by Dewey, Carriou & Smits (2012), who concluded that the presence of two vortex pairs result in two separate peaks in the mean profile. The Strouhal number  $St = 0.29$  (figure 5e), initially produces a 2P wake with mean profiles that are trapezoidal ( $0.22 \leq x/c \leq 1.5$ ). These

## Connections between propulsive efficiency and wake structure

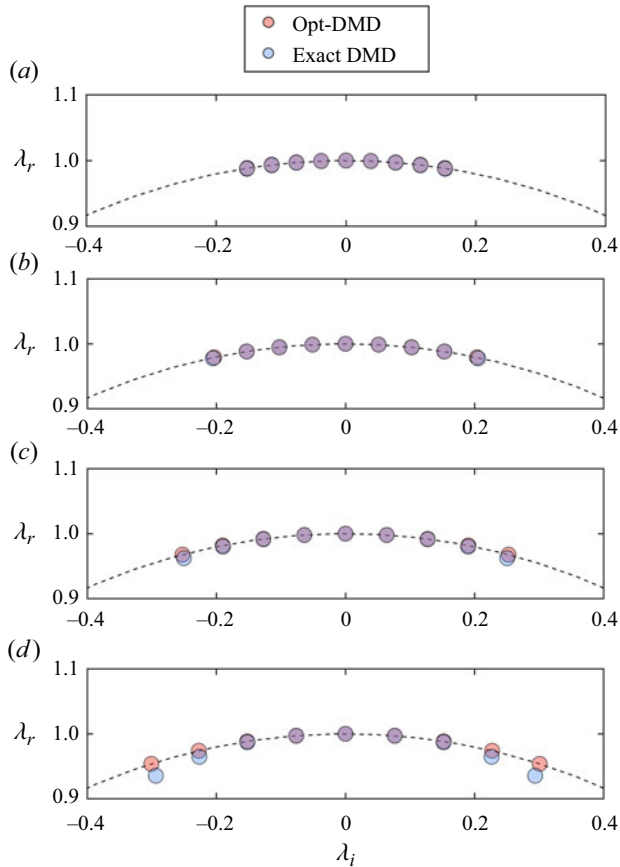


Figure 6. Eigenvalue spectrum for (a)  $St = 0.16$ , (b)  $St = 0.23$ , (c)  $St = 0.29$ , (d)  $St = 0.35$ . Purple markers indicate overlap of the opt-DMD (red) and DMD (blue) eigenvalues. Here  $\lambda_r$  denotes the real component of the eigenvalues while  $\lambda_i$  denotes the imaginary component.

vortex pairs coalesce further downstream to a 2S wake, creating a mean profile resembling that produced by a single jet ( $1.5 < x/c \leq 2.7$ ). As the Strouhal number increases further to  $St = 0.35$ , a classical 2S wake is observed, suggesting a transition from a 2P to 2S wake structure over the range  $0.23 < St < 0.35$ . These observations are consistent with the results of Moored *et al.* (2012), who found optimal efficiencies in both wake types.

### 4.3. Modal decomposition

We now compare results between the exact-DMD and opt-DMD algorithms. Eigenvalues obtained for the first nine DMD modes for both methods are shown in figure 6. The mode corresponding to  $\lambda = 0$  for each Strouhal number represents the mean flow field, while the other eigenvalues, having a non-zero imaginary part, represent the time-periodic modes. Note that the eigenvalues with non-zero imaginary components are represented in complex conjugate pairs (i.e. with  $\lambda_k = \lambda_{k,r} \pm \lambda_{k,i}$ ), which together represent a single-frequency component of the flow field.

As shown by Magionesi *et al.* (2018), the eigenvalue problem degenerates and results in harmonic solutions when the dominant components of the flow travel at a constant speed, and with constant shape. This is noticeable in both the opt-DMD and exact-DMD modes,

whereby the eigenvalues have oscillation frequencies ( $|\omega_{k,i}|$ ) that are multiples of the first harmonic. The opt-DMD eigenvalues for all Strouhal numbers lie directly on the unit circle, suggesting that the modes neither grow or decay overtime ( $|\lambda_k| = 1$ ). In contrast, the exact-DMD eigenvalues tend to fall within the circle for increasing  $St$ , particularly for large values of  $|\lambda_{k,i}|$ , signifying that the oscillatory modes obtained via exact-DMD decay over time ( $|\lambda_k| < 1$ ). This is most evident for the largest Strouhal number case ( $St = 0.35$ ) in [figure 6\(d\)](#), which shows eigenvalues within the unit circle for  $|\lambda_{k,i}| > 0.2$ . Similar trends were reported by Bagheri (2014), who observed that eigenvalue damping increases linearly with noise amplitude and quadratically with frequency. For the remainder of this paper, we refer to the flow field produced by the dynamic modes associated with a complex conjugate pair of eigenvalues as a single mode, and consider the first to fourth harmonics as modes 1–4.

To further understand the effects of mode decay via eigenvalue damping, we computed the periodogram-based power spectral density of the original flow field and the reconstructed flow from opt-DMD and exact-DMD modes (see [figure 7](#)). Note that each of the peaks represents the flow field produced by a pair of dynamic modes (i.e. corresponding to a complex conjugate pair of eigenvalues). The normalized frequencies for these peaks,  $St = fA_{TE}/U_\infty$ , represent harmonics of the foil oscillation frequency. The power from the exact-DMD reconstruction are lower in power compared with the opt-DMD reconstruction and full flow field ([figure 7c,d](#)). This decay can be attributed to the dampened eigenvalues from the exact-DMD algorithm, observed in [figure 6\(c,d\)](#). As a result, the effect of reduced power worsens with increasing  $St$ . These results suggest that the opt-DMD algorithm outperforms the exact-DMD method in retaining the energy in all modes, as also shown by Strom *et al.* (2022).

For completeness, we also highlight the exponential decay of the amplitude peaks of the opt-DMD modes, as shown by the dotted lines in [figure 7](#). Interestingly, the exponential fits for  $St = 0.16$  and  $St = 0.23$  show some flattening at the higher frequencies, suggesting that the wake is not strongly locked to the actuation frequency for these cases. For example, in the case of  $St = 0.23$  ([figure 7b](#)), the third opt-DMD and exact-DMD modes have a slightly higher energy ( $-10.9$  dB and  $-12.9$  dB) compared with mode two ( $-11.1$  dB and  $-14.0$  dB). The other cases do not show this behaviour.

#### 4.3.1. Opt-DMD coherent structures

In addition to characterizing oscillation frequencies and growth or decay rates, DMD also provides insight into the wake structure. Reconstructions for the first two modes are shown in [figure 8](#). Each modal reconstruction corresponds to the phase of oscillation shown in [figure 5](#). For all  $St$  values, mode 1 exhibits top–bottom symmetry in vortex structure across the centreline ( $y/c = 0$ ). In contrast, mode 2 has an antisymmetric structure with vortex lobes of smaller size compared with mode 1. The higher-order modes 3 and 4 are also symmetric and asymmetric, respectively, as shown in [figure 9](#). Qualitatively, these modes better capture skews in the wake structure across the centreline, particularly for the case of  $St = 0.16$  ([figure 9a,b](#)).

It was shown by Moored *et al.* (2012) that the overlap in vorticity modes at certain locations in space contributes to producing the full vortex structure. Similar observations can also be made in the present study, where the modal hierarchy is trying to represent a convective process in terms of purely oscillatory DMD modes that are harmonics of the flapping frequency. This is reflected in the DMD mode structure: since mode 2 exhibits twice the oscillation frequency as mode 1, vortex lobes from mode 2 exhibit roughly twice

Connections between propulsive efficiency and wake structure

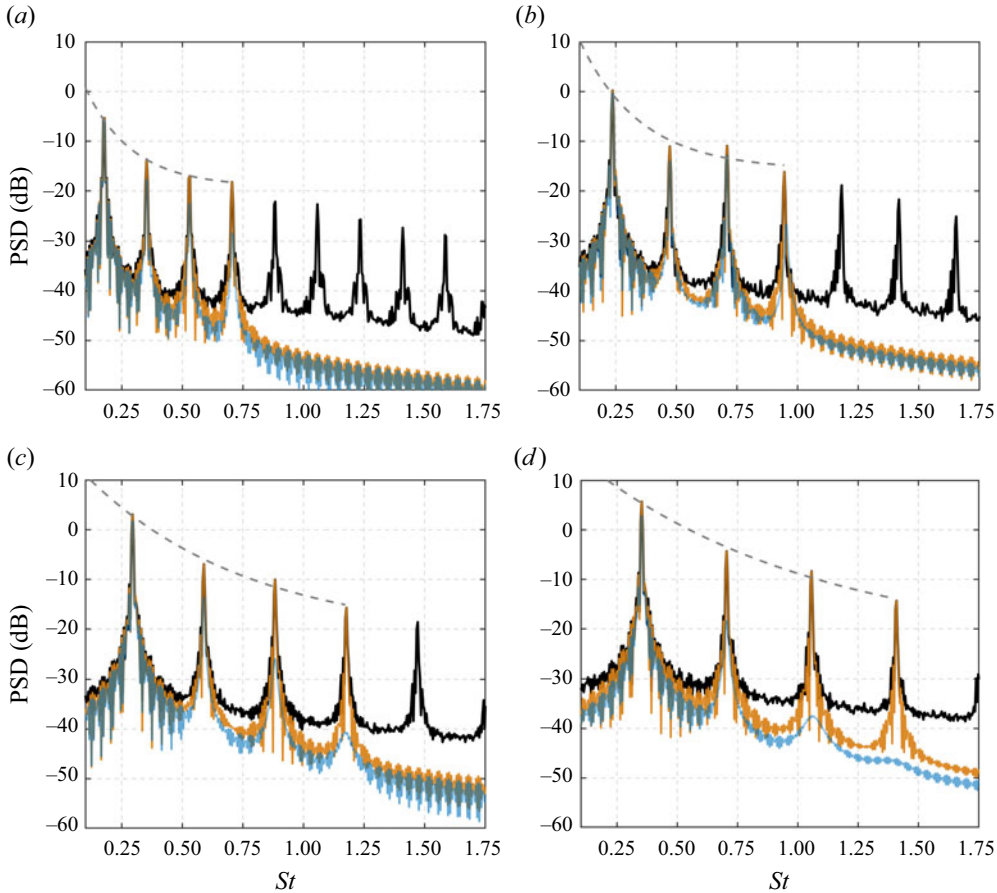


Figure 7. Power spectral densities for the original flow field (black) and the reconstructed flow fields from the opt-DMD (orange) and exact-DMD (blue) method for (a)  $St = 0.16$ , (b)  $St = 0.23$ , (c)  $St = 0.29$  and (d)  $St = 0.35$ . The dotted lines represent exponential decay rates from fits to the first four mode amplitudes from opt-DMD and show the following behaviour: (a)  $e^{-5.1St}$ , (b)  $e^{-4.0St}$ , (c)  $e^{-1.5St}$  and (d)  $e^{-1.0St}$ .

the spatial wavenumber as mode 1 (see figure 8). A coherent vortex is formed at a particular region in space when both modes are either in-phase or in anti-phase and vortex lobes with the same sign overlay each other. This is also consistent with the fact that the foil sheds a vortex each half-cycle. Whether the vortex formed is positive or negative is determined by the sign of the spatial eigenfunctions. These features (and the modes themselves) are phase-locked in a reference frame moving with the local convective velocity.

Notable differences between the modes from the near-momentumless wake and that from the 2P and 2S wakes are observed. For instance, mode 1 for  $St = 0.16$  has approximately four symmetric lobes of vorticity along the lateral axis (figure 8a). These elongated vortex packets expand laterally as they advect downstream and similar trends can be seen for mode 2 (figure 8b). This is consistent with the lateral variation observed in the mean velocity profile and phase-averaged vorticity fields. In contrast, mode 1 for the cases  $St = 0.23$ ,  $0.29$  and  $0.35$  primarily consists of two vortex lobes with decreasing streamwise extent. Thus, the size of the lobes reflects the length scale of the shed vortices, which is partially determined by the convective length scale  $U_\infty/f$ .

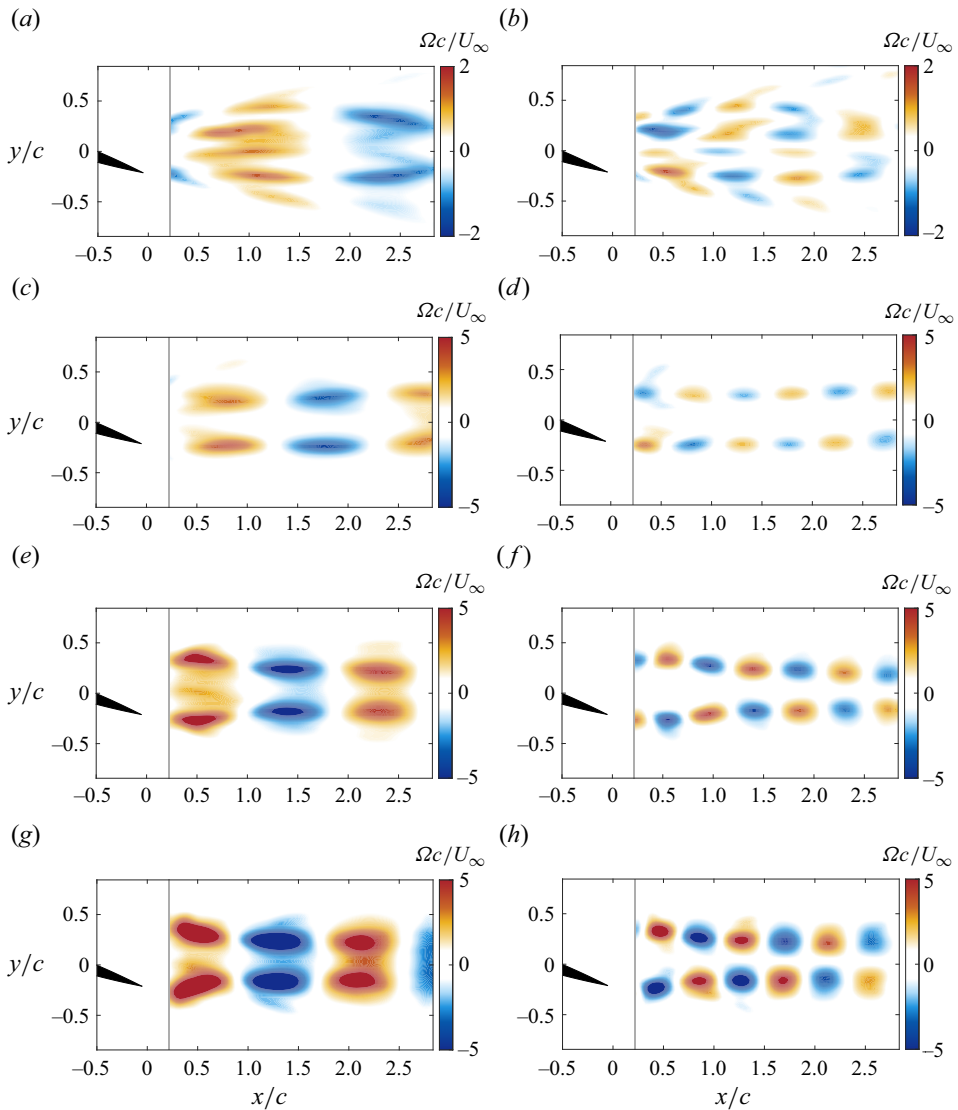


Figure 8. Vorticity fields from opt-DMD modes 1 (*a,c,e,g*) and 2 (*b,d,f,h*) for (*a,b*)  $St = 0.16$ , (*c,d*)  $St = 0.23$ , (*e,f*)  $St = 0.29$  and (*g,h*)  $St = 0.35$ . See also supplementary movie 2 and movie 3 available at <https://doi.org/10.1017/jfm.2024.446>.

The differences that reflect the transition from the 2P wake to the 2S reverse von Kármán street are more subtle. In the case of  $St = 0.23$ , which exhibits a 2P wake morphology, the vorticity lobes travel consistently downstream (see figure 8*c,d*). As the Strouhal number increases from  $St = 0.23$  to  $St = 0.35$ , the lobe pairs move inward towards the centreline over the region  $0.22 \leq x/c \leq 1.0$ . In the region where  $x/c > 1.0$ , the lobes consistently travel in the streamwise direction again. This dynamic characteristic can be observed better from modes 3 and 4 in figures 9(*c*)–9(*h*), where the lobes structures are considerably smaller. Another key distinction across the 2P to 2S wake transition is that the symmetric vorticity lobes of modes 1 and 3 start to coalesce into a single lobe towards the downstream end of the field of view,  $x/c \geq 2.0$ . The antisymmetric pairs for

Connections between propulsive efficiency and wake structure

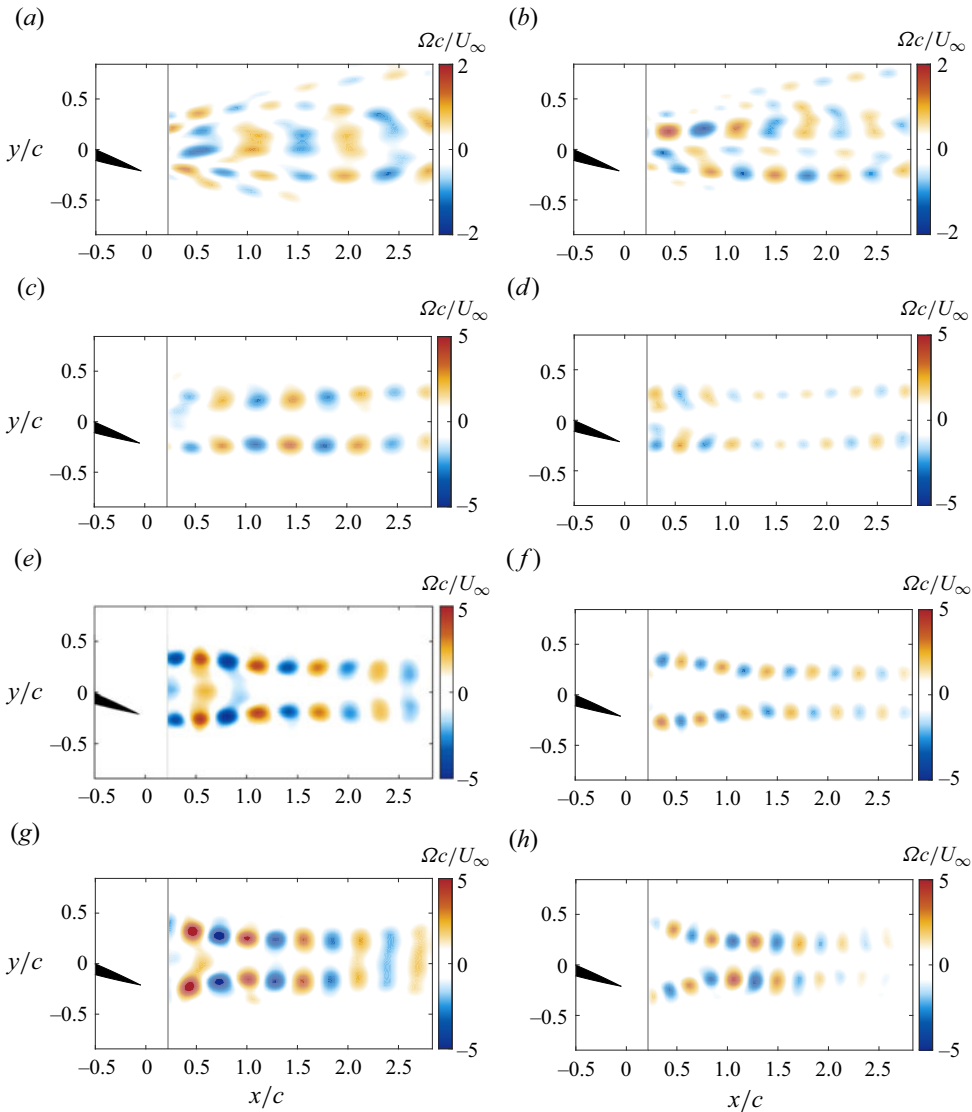


Figure 9. Vorticity fields from opt-DMD modes 3 (a,c,e,g) and 4 (b,d,f,h) for (a,b)  $St = 0.16$ , (c,d)  $St = 0.23$ , (e,f)  $St = 0.29$  and (g,h)  $St = 0.35$ . See also supplementary movie 4 and movie 5 available at <https://doi.org/10.1017/jfm.2024.446>.

modes 2 and 4 remain apart. This is most noticeable for the case of  $St = 0.35$  (figures 8g and 9g).

Although the high-frequency wake structures exhibit reverse von Kármán streets – as expected for thrust-producing systems – their symmetric and antisymmetric topologies are similar to that from the classical Kármán vortex street shed from two-dimensional objects (Tu *et al.* 2014; Araya *et al.* 2017; Taira *et al.* 2020). In these drag-producing wakes, the dominant DMD or POD modes obtained for these flows can also correspond to a series of frequency harmonics. One distinction from the classical drag-producing bluff body wakes is that their symmetric mode structures may consist of a single lobe of vorticity across the  $y$  axis – as shown in experiments from Tu *et al.* (2014) – rather than two or more from our study.

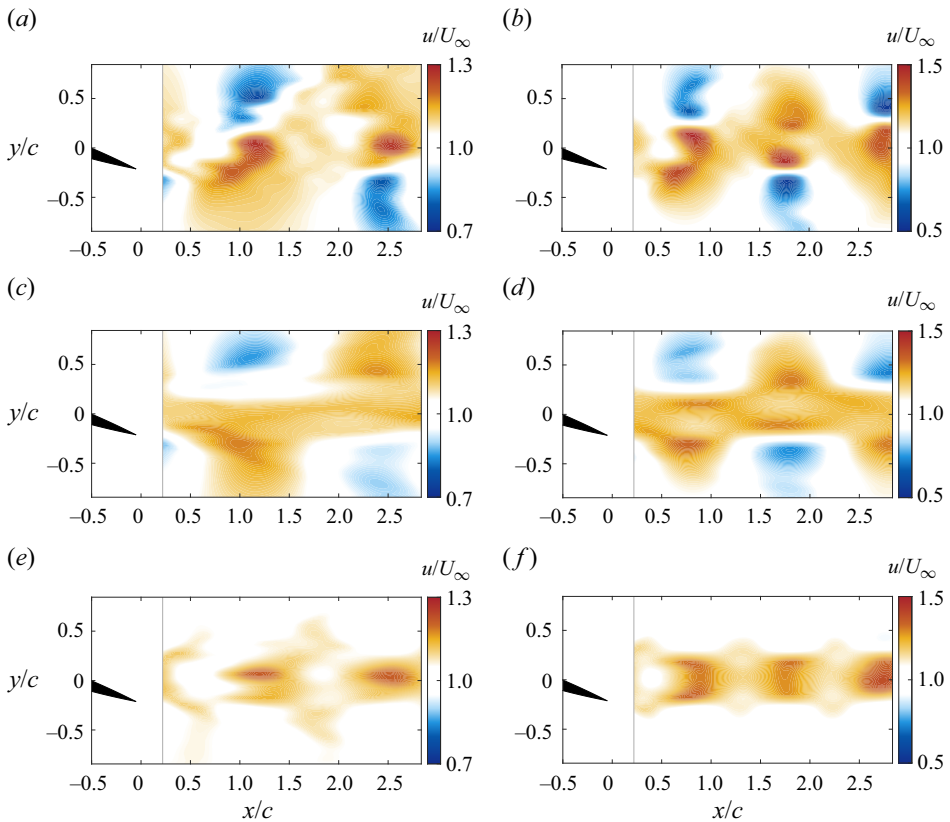


Figure 10. Reconstructed streamwise velocity fields:  $u = \bar{u} + \sum_{n=1}^4 \tilde{u}_n$  (a,b);  $\bar{u} + \tilde{u}_1$  (c,d) and  $\bar{u} + \tilde{u}_2$  (e,f). The left and right columns are of the Strouhal numbers  $St = 0.16$  and  $St = 0.23$ , respectively. The mode hierarchy is in terms of frequency, with the lowest corresponding to mode 1.

#### 4.3.2. Influence of modes on wake dynamics

To further understand how the symmetric and antisymmetric modes relate to the full flow field, we superimpose the streamwise component associated with DMD modes 1 ( $\tilde{u}_1$ ) and 2 ( $\tilde{u}_2$ ) separately with the time-averaged streamwise velocity ( $\bar{u}$ ). Figures 10 and 11 show the full opt-DMD reconstructions (i.e. comprising modes 1–4) as well as these single-mode reconstructions of the streamwise velocity component. In the original streamwise fields the vortex development is characterized by the regions where  $u$  is less than that of the free-stream velocity ( $u/U_\infty < 1$ ), resulting in shear layer roll up. In the transition to the 2S wake, a wavy jet is observed in the original flow fields (11a,b). Mode 1 with the mean flow ( $u = \bar{u} + \tilde{u}_1$ ) reproduces most of these wake dynamics, including a reasonable portion of the shear layer roll up from which the vortices emerge.

The wake dynamics associated with mode 1 and the associated symmetric vorticity perturbations closely resemble the spatial instabilities observed by Moored *et al.* (2012) in the 2S wake structure created by a flexible fin. The main distinction lies in the number of vorticity lobes, with the former exhibiting two lobes instead of three. This observation suggests that the opt-DMD modes yield coherent structures that are related to spatial instabilities. It is also likely that mode 1 induces a majority of the net thrust since this mode is associated with the lower velocity structures that form the vortex structures outside the central jet. In contrast, mode 2 is associated with the shedding frequency of each vortex or

## Connections between propulsive efficiency and wake structure

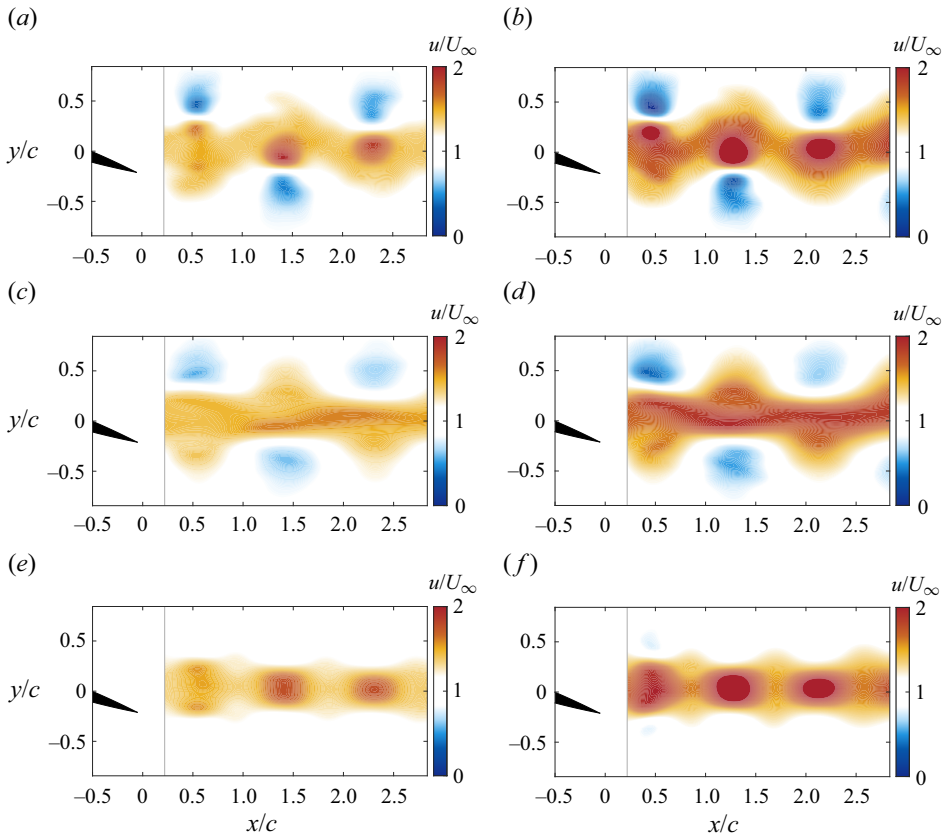


Figure 11. Reconstructed streamwise velocity fields:  $u = \bar{u} + \sum_{n=1}^4 \tilde{u}_n$  (a,b);  $\bar{u} + \tilde{u}_1$  (c,d) and  $\bar{u} + \tilde{u}_2$  (e,f). The left and right columns are of the Strouhal numbers  $St = 0.29$  and  $St = 0.35$ , respectively. The mode hierarchy is the same as in figure 10.

vortex pair for the 2S and 2P wakes (i.e. twice the oscillation frequency). Mode 2 accounts for much of the remaining shear in the centre jet region; this is particularly evident in the higher Strouhal number wakes (figure 11e,f).

### 4.3.3. Coherent Reynolds stress contributions from DMD modes

The subtle differences in DMD mode structure across Strouhal numbers suggest that the associated Reynolds shear stresses may provide additional insight into thrust and drag effects. Following Reynolds & Hussain (1972) and assuming that the Reynolds stress contributions from the turbulent fluctuations  $\mathbf{u}'$  are negligible compared with the contributions from the phase-averaged periodic components  $\tilde{\mathbf{u}}$ , the time-averaged momentum equation in the streamwise direction can be expressed as follows:

$$\bar{u} \frac{\partial \bar{u}}{\partial x} + \bar{v} \frac{\partial \bar{u}}{\partial y} \approx \frac{\partial}{\partial y} \left[ \nu \left( \frac{\partial \bar{u}}{\partial y} \right) - \overline{\tilde{u} \tilde{v}} \right]. \quad (4.2)$$

The equation above also assumes no external pressure gradient, a purely two-dimensional flow, and that cross-stream gradients of the viscous and Reynolds stress terms dominate over the streamwise gradients. Invoking both a strong parallel flow assumption, whereby

$\bar{v} \approx 0$  and  $\partial \bar{u} / \partial x \approx 0$  locally, (4.2) can be further simplified to

$$v \frac{d^2 \bar{u}_n}{dy^2} \approx \frac{d\bar{u}_n \bar{v}_n}{dy}, \quad (4.3)$$

which can be used to estimate the induced mean flow. In the above equation,  $\bar{u}_n$  can be thought of as the mean velocity induced by DMD mode  $n$ , i.e. the Reynolds shear stresses generated by the periodic velocity components  $\tilde{u}_n$  and  $\tilde{v}_n$  associated with mode  $n$ . Since the DMD modes are harmonics of the foil oscillation frequency, there are no mean Reynolds shear stress contributions from interactions across modes. In other words, we expect  $\bar{u}_m \bar{v}_n = 0$  for  $m \neq n$ . Equation (4.3) indicates that positive values of  $d\bar{u}_n \bar{v}_n / dy$  are associated with minima in  $\bar{u}_n$  and *vice versa*. Positive  $\bar{u}_n$  contributions increase momentum in the wake and produce thrust. The opposite is true for negative  $\bar{u}_n$  contributions, which result in induced drag.

Predictions made using the highly simplified momentum balance in (4.3) are complementary to the control volume analyses of momentum entrainment and expulsion presented by Moored *et al.* (2014), which showed that the surrounding fluid is entrained into the near-wake region close the foil at wake resonance. The increase in mass flow rate of the jet wake produces thrust, and the entrainment region should therefore have a Reynolds stress distribution in which the periodic components  $\bar{u}\bar{v}$  induce a jet-like mean profile. We solve (4.3) numerically for  $\bar{u}_n$  using the Reynolds shear stress profiles for DMD modes 1 and 2 that are closest to the foil ( $x/c = 0.22$ ), enforcing the boundary conditions  $\bar{u}_n(-\infty) = \bar{u}_n(\infty) = 0$ .

Figures 12 and 13 respectively show the coherent Reynolds stress fields  $\bar{u}_n \bar{v}_n$  and induced mean profiles  $\bar{u}_n$  predicted using (4.3) for opt-DMD modes 1 and 2. The Reynolds stress fields show patterns that are antisymmetric across the centreline over the region of  $0.22 < x/c < 1.0$ . This antisymmetry begins to break down for the case of  $St = 0.35$  (figures 12g and 13g). As expected, mode 1 (i.e. the primary harmonic) generates larger Reynolds shear stresses and induced mean flow contributions compared with mode 2. However, this discrepancy is more pronounced for the higher Strouhal number cases ( $St = 0.29, 0.35$ ) exhibiting 2S-type wakes. The maximum magnitudes of  $\bar{u}_1 \bar{v}_1$  for mode 1 increase with Strouhal number.

The shape of the induced mean flow profiles for mode 1 are similar for the  $St = 0.16$  and  $0.23$  cases (figure 12b,d), where two distinct positive maxima can be seen (with one noticeable negative component for the case  $St = 0.23$ ). Induced mean profiles for both 2S wakes ( $St = 0.29, 0.35$ ) in 12(f,h) also show similar characteristics. However,  $\bar{u}_1$  for  $St = 0.29$  shows two separate maxima while the profile for  $St = 0.35$  shows a single maximum near the centreline. This transition from two distinct maxima in the mean profile to a single peak is consistent with the 2P-2S transition noted earlier as the Strouhal number increases from  $St = 0.23$  to  $St = 0.35$ . Interestingly,  $\bar{u}_1$  profiles for  $St = 0.29$  and  $St = 0.35$  match the measured mean profile shapes shown in figure 5(c,d). Specifically, the  $St = 0.29$  profile is approximately trapezoidal in shape while the  $St = 0.35$  profile resembles a typical jet. Induced  $\bar{u}_1$  profiles for these high Strouhal number cases are also much larger in magnitude compared with the lower Strouhal number cases ( $St = 0.16, 0.23$ ), which is indicative of higher entrainment and thrust production.

Generally, Reynolds shear stress contributions and induced velocities from mode 2 in figure 13 are lower than those from mode 1. Particularly,  $\bar{u}_2 \ll \bar{u}_1$  for the 2S wakes in  $St = 0.29$  and  $St = 0.35$ . Additionally, while the mode 1 contributions vary significantly in magnitude across Strouhal number, all of the mode 2 profiles exhibit similar maximum values of  $\bar{u}_2 \bar{v}_2$  and  $\bar{u}_2$ . Reynolds stress fields associated with mode 2 for  $St = 0.16$  and

Connections between propulsive efficiency and wake structure

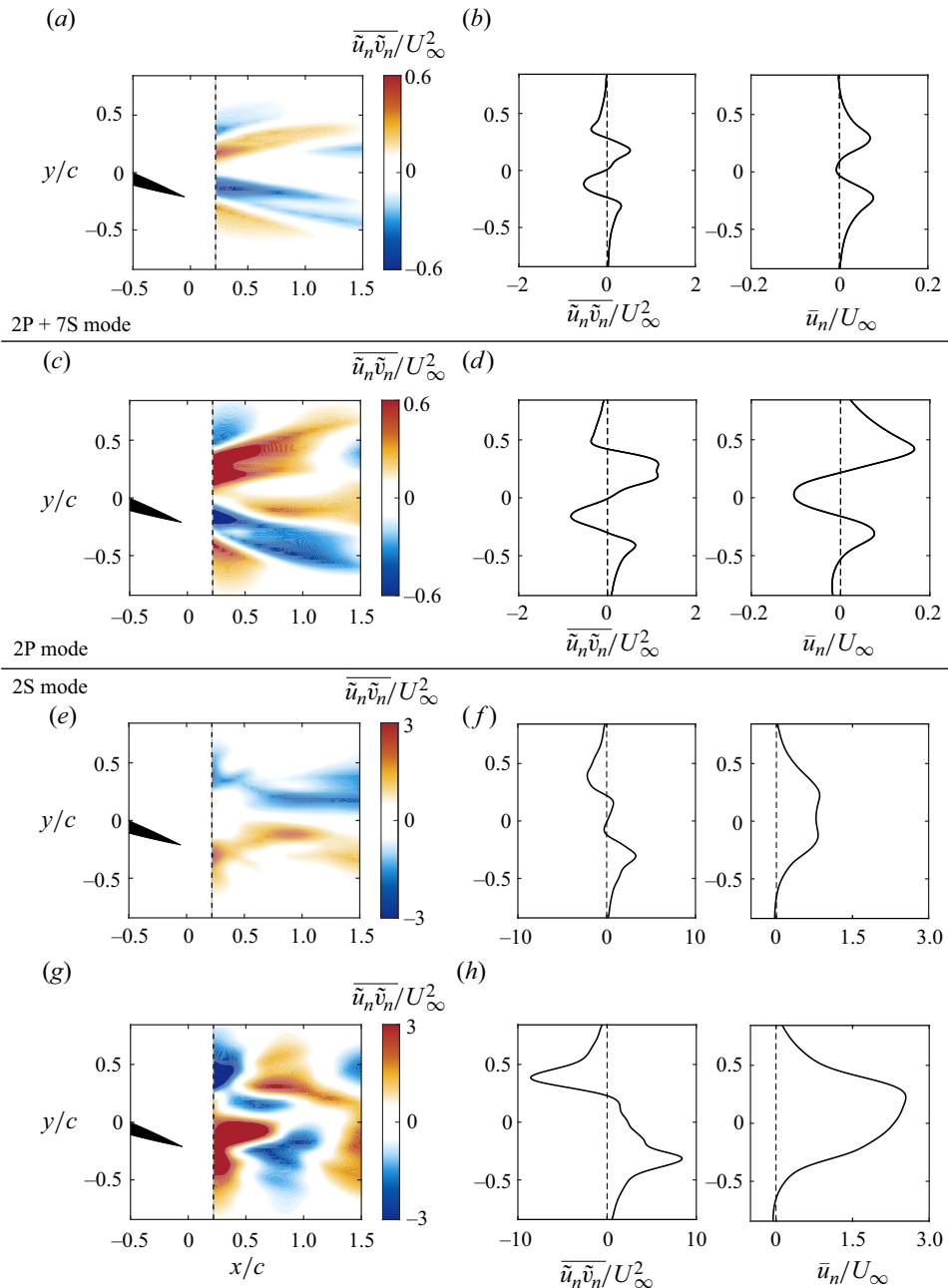


Figure 12. Mean Reynolds stress fields  $\overline{\tilde{u}_1 \tilde{v}_1}$  and induced mean flow profiles  $\bar{u}_1$  ( $x/c = 0.22$ ) for opt-DMD mode 1 at (a,b)  $St = 0.16$ , (c,d)  $St = 0.23$ , (e,f)  $St = 0.29$  and (g,h)  $St = 0.35$ .

$St = 0.23$  (figure 13b,d) remain reasonably coherent over the field of view. The resulting mean flow profiles also show consistent negative values ( $\bar{u}_2 < 0$ ), which is indicative of drag generation. This aligns with Floryan *et al.* (2017), who found that scaling laws differed from experiments in efficiency due to viscous drag effects at lower Strouhal numbers. The coherent stress fields are likely characteristics of the transition to bluff body shedding.

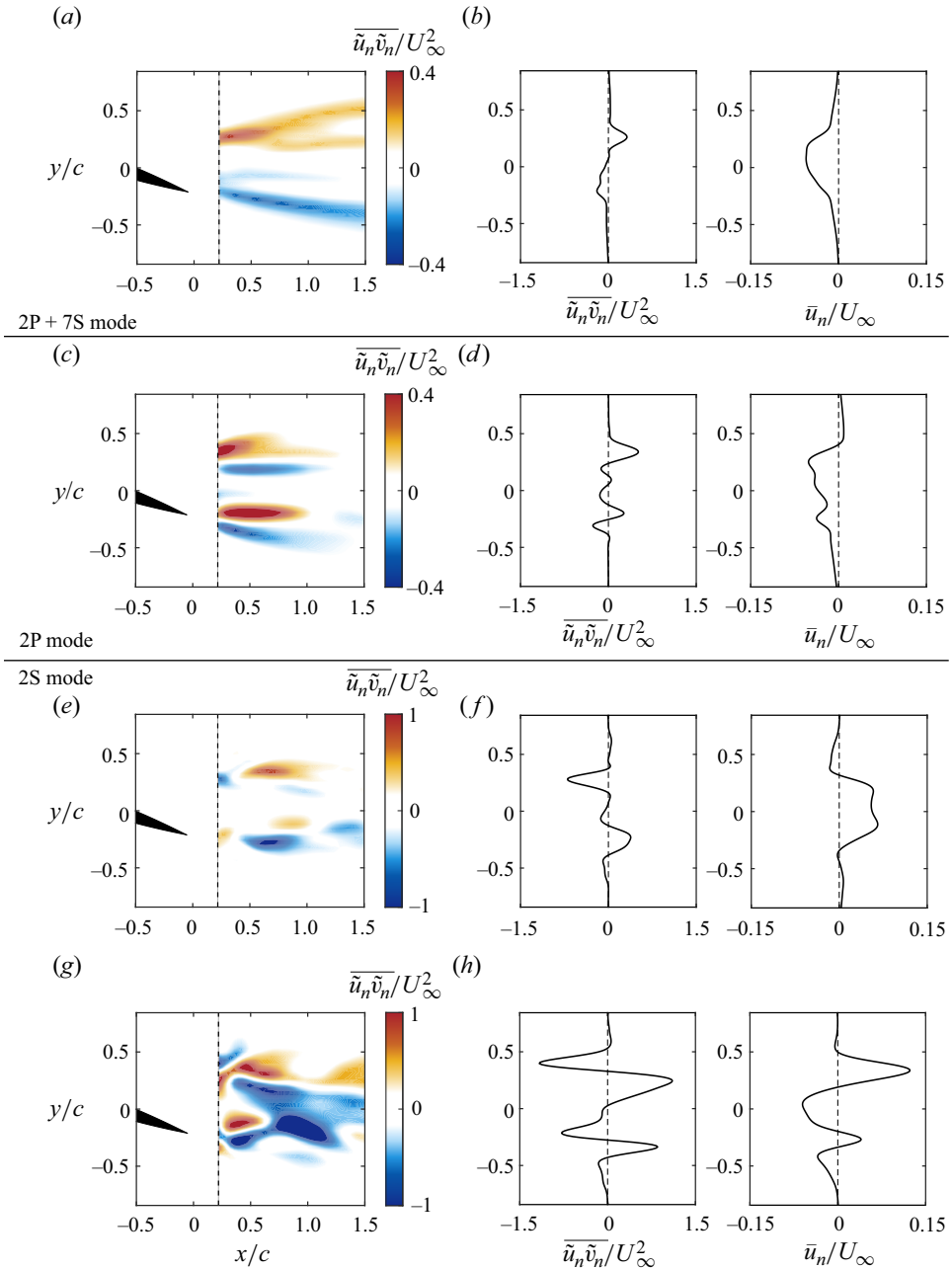


Figure 13. Mean Reynolds stress fields  $\overline{\tilde{u}_2 \tilde{v}_2}$  and induced mean flow profiles  $\bar{u}_2$  ( $x/c = 0.22$ ) for opt-DMD mode 2 at (a,b)  $St = 0.16$ , (c,d)  $St = 0.23$ , (e,f)  $St = 0.29$  and (g,h)  $St = 0.35$ .

Note that these drag-inducing effects are characterized by modes with a higher frequency than that from typical bluff body shedding (cf. similar observations from Strom *et al.* 2022).

While the  $\bar{u}_2$  profiles are primarily negative for the lower Strouhal number cases, distinct positive regions are observed as the flow transitions from a 2P wake to a 2S wake for

$St = 0.29$  and  $0.35$  as seen in [figure 13\(f,h\)](#). For  $St = 0.29$ , the  $\bar{u}_2$  profile is positive and approximately trapezoidal in shape, matching the mean flow in [figure 5\(f\)](#). For  $St = 0.35$ , the induced  $\bar{u}_2$  profile has a mix of positive and negative regions, with the total area under the profile yielding a net negative value. The transition from purely negative  $\bar{u}_2$  contributions for  $St = 0.16$  and  $0.23$  to primarily positive  $\bar{u}_2$  contributions for  $St = 0.29$  is reminiscent of the earlier convective instability work – as noted by Triantafyllou *et al.* (1993), in a reverse von Kármán vortex street, there is little to no competition between the drag wake and the thrust wake. This is consistent with the present observations for  $St = 0.29$ .

#### 4.4. Deterioration of propulsive efficiency at high $St$

The marginal deterioration in propulsive efficiency along with the negative  $\bar{u}_2$  contributions for the  $St = 0.35$  case can potentially be attributed to effects from leading-edge vortices. While we do not have access to PIV data around the foil, force and torque measurements, along with the angle of attack trends support this interpretation. In particular, we expect these effects to be evident in the normal or lift forces on the foil, which also influence the power input and propulsive efficiency (see [\(2.4a,b\)](#) and [\(2.5\)](#)). Dimensionless phase-averaged lift forces  $F_y$  and power requirements  $\wp$  measured for Strouhal numbers  $St = 0.29$ – $0.59$  are shown in [figure 14](#). As expected, the lift forces exhibit the same oscillation frequency as the actuation, which also matches the first mode frequencies. The relative power exhibits oscillations at twice the actuation frequency, which is also the second mode frequency.

Noticeable deviations in relative lift and power are observed between the near-optimal Strouhal numbers ( $St = 0.29$  and  $0.35$ ) and the highest Strouhal number case ( $St = 0.59$ ). Particularly, the small enhancements in the magnitude of the lift force observed between  $t/T \approx 0.4$ – $0.5$  and  $t/T \approx 0.9$ – $1.0$  lead to lower relative power requirements, as shown in [figure 14\(b,c\)](#). For the highest propulsive efficiency case of  $St = 0.29$ , additional decreases in relative power at  $t/T \approx 0.25$  and  $0.75$  lower the overall power across the full oscillation cycle ([figure 14c](#)). Note that the relative lift force enhancements for this Strouhal number case appear soon after maxima and minima in the effective angle of attack ( $t/T = 0.25, 0.75$ ).

These relative lift force enhancements may be linked to the structure of the Reynolds shear stress contribution and positive induced velocity from DMD mode 2 for  $St = 0.29$  ([figure 13e,f](#)), suggesting a delay in separation of the leading-edge vortices. The separation effects may start to occur for the  $St = 0.35$  case, which show a negative induced velocity from mode 2 ([figure 12h](#)) and higher relative power requirements in comparison to those from  $St = 0.29$ , resulting in lower propulsive efficiency. The deterioration in performance is even more visible for the  $St = 0.59$  case, which shows a substantial decrease in the magnitude of  $F_y/F_{y0}$  and corresponding increases in  $\wp/\wp_0$ .

The tapering of efficiency past  $St = 0.29$  can also be explained based on high angles of attack. The stall angle for a static NACA 0012 foil is approximately  $16^\circ$ . However, oscillating loads can increase the stall angle substantially (Maresca, Favier & Rebont 1979). For the present experiments, the maximum angles of attack  $\alpha_0$  for the higher Strouhal number cases  $St = 0.29, 0.35$  and  $0.59$  are  $28.2^\circ, 33.1^\circ$  and  $47.5^\circ$ , respectively. Thus, it is likely that the induced drag effects from the secondary mode ([figure 13h,f](#)) become more relevant as the effective angle of attack increases, through which separation effects may occur – as also evident in the  $F_y/F_{y0}$  traces. In turn, the efficiency tapers downward past the Strouhal number  $St = 0.29$ . However, it would be misleading to say that all cases with high angles of attack lead to reduced efficiency, as some combinations of

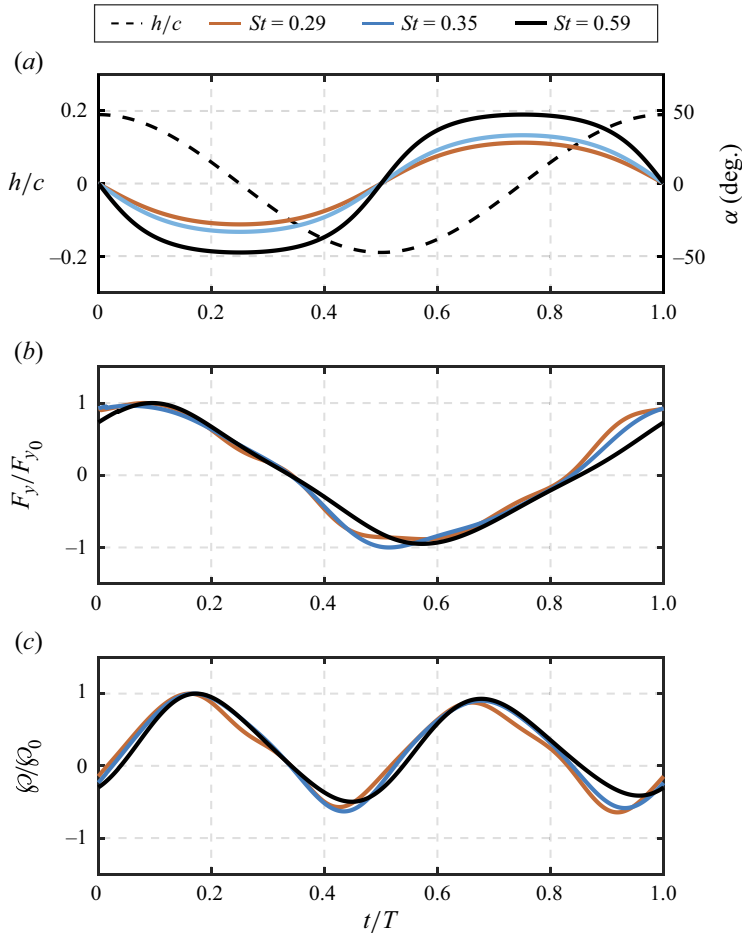


Figure 14. Dimensionless heave cycle  $h/c$  (dotted line) and effective angle of attack  $\alpha$  (solid lines) for one cycle (a), together with phase-averaged lift forces  $F_y$  (b) and power requirements  $\varphi$  (c) normalized by maximum values ( $F_{y0}$  and  $\varphi_0$ ) for  $St = 0.29$  (red),  $St = 0.35$  (blue) and  $St = 0.59$  (black).

kinematic parameters can delay these dynamic stall effects (Maresca *et al.* 1979; Ellington *et al.* 1996; Anderson *et al.* 1998). Instead, a high angle of attack where the flow stays attached to the foil can potentially maximize efficiency, an effect that has also been observed for flexible propulsors (Quinn *et al.* 2015).

## 5. Discussion and conclusions

A triple decomposition method in which the periodic component of the wake is composed of opt-DMD modes was used to provide further physical insight into the propulsive performance of oscillating foils. The experimental data in which the method was used are broadly consistent with prior literature. We observe a near-momentumless wake structure for  $St = 0.16$  and peak propulsive efficiency for  $St = 0.29$ . Over this range of Strouhal numbers, PIV measurements show a transition from a momentumless wake to a 2S wake morphology associated with the classical reverse von Kármán vortex street. The opt-DMD method is employed here instead of the classical or (exact) DMD approach as it captures more energy in the periodic component of the flow field. For this particular foil, the

opt-DMD modes appear as harmonics of the foil oscillating frequency, with alternating symmetric and antisymmetric morphology across the wake centreline.

The most interesting finding from our study is the relationship between the coherent Reynolds stress contributions from DMD modes and their impact on propulsive performance. Although (4.3) is only an approximation to the mean flow equation for the wake, it helps delineate modal contributions to drag and thrust. In our experiments, the mean velocities induced by the primary opt-DMD mode (mode 1) generally show thrust-producing characteristics across all  $St$  values, though there is a transition from a two-hump mean profile for the 2P wakes to a jet-like mean profile for the 2S wakes. However, several different trends emerge from the mean velocities induced by mode 2, representing features oscillating at twice the fundamental frequency of the foil: (i) for Strouhal numbers below the optimum ( $St < 0.29$ ), the induced mean velocities  $\bar{u}_2$  are negative and suggest a transition to bluff body shedding; (ii) the secondary mode for the optimum Strouhal number case ( $St = 0.29$ ) has a prominent positive induced mean velocity, indicating that the thrust wake is dominant; (iii) past the optimum Strouhal number, mode 2 transitions back to a negative induced mean velocity, which may be indicative of flow separation as a result of high angles of attack ( $St > 0.29$ ).

Given the close connection between DMD and stability analyses, it may be of interest to compare the opt-DMD modes with features identified in prior stability analyses (Moored *et al.* 2012; Arbie *et al.* 2016). The development of the opt-DMD modes close to the foil suggest that their may be some spatial growth of these perturbations in the near field. Thus, there may be links between these opt-DMD modes and the spatially growing modes identified in the ‘wake resonance’ studies (Triantafyllou *et al.* 1993; Lewin & Haj-Hariri 2003; Moored *et al.* 2014). Nonetheless, it should be emphasized that the temporal DMD method was used in this study, which extracts modes at a particular oscillation frequency. A spatial DMD approach could provide a more direct approach to understanding these instability mechanisms. In this case, a spatial resolution that is higher than the PIV data collected in this study would be necessary to allow for an appropriate spatial DMD analysis.

This study focused on a narrow parameter range: we studied a single, rigid foil exhibiting periodic single-frequency oscillations. However, modal analysis methods similar to those employed here could provide substantial insights into wakes involving more complex kinematics, dynamic fluid–structure interactions, multiple-foil interactions or massively separated flows (see, e.g. Raspa, Godoy-Diana & Thiria 2013; Andersen *et al.* 2017).

**Supplementary movies.** Supplementary movies are available at <https://doi.org/10.1017/jfm.2024.446>.

**Funding.** This material is based on work supported by the National Science Foundation under grant no. 1943105. The authors thank Professor G. Spedding and S. Brunton for insightful discussions, as well as the reviewers for their constructive feedback on this paper.

**Declaration of interests.** The authors report no conflict of interest.

#### Author ORCIDs.

-  Morgan R. Jones <https://orcid.org/0009-0004-7872-986X>;
-  Eva Kanso <https://orcid.org/0000-0003-0336-585X>;
-  Mitul Luhar <https://orcid.org/0000-0002-7970-9762>.

#### REFERENCES

- ANDERSEN, A., BOHR, T., SCHNIPPER, T. & WALTHER, J.H. 2017 Wake structure and thrust generation of a flapping foil in two-dimensional flow. *J. Fluid Mech.* **812**, R4.

- ANDERSON, J.M., STREITLIEN, K., BARRETT, D.S. & TRIANTAFYLLOU, M.S. 1998 Oscillating foils of high propulsive efficiency. *J. Fluid Mech.* **360**, 41–72.
- ARAYA, D.B., COLONIUS, T. & DABIRI, J.O. 2017 Transition to bluff-body dynamics in the wake of vertical-axis wind turbines. *J. Fluid Mech.* **813**, 346–381.
- ARBIE, M.R., EHRENSTEIN, U. & ELOY, C. 2016 Stability of momentumless wakes. *J. Fluid Mech.* **808**, 316–336.
- ASKHAM, T. & KUTZ, J.N. 2018 Variable projection methods for an optimized dynamic mode decomposition. *SIAM J. Appl. Dyn. Syst.* **17** (1), 380–416.
- BAGHERI, S. 2014 Effects of weak noise on oscillating flows: linking quality factor, Floquet modes, and Koopman spectrum. *Phys. Fluids* **26** (9), 094104.
- BAJ, P., BRUCE, P.J.K. & BUXTON, O.R.H. 2015 The triple decomposition of a fluctuating velocity field in a multiscale flow. *Phys. Fluids* **27** (7), 075104.
- BEAL, D.N., HOVER, F.S., TRIANTAFYLLOU, M.S., LIAO, J.C. & LAUDER, G.V. 2006 Passive propulsion in vortex wakes. *J. Fluid Mech.* **549** (1), 385–402.
- BRYANT, M., MAHTANI, R.L. & GARCIA, E. 2012 Wake synergies enhance performance in aeroelastic vibration energy harvesting. *J. Intell. Mater. Syst. Struct.* **23** (10), 1131–1141.
- DAWSON, S.T.M., HEMATI, M.S., WILLIAMS, M.O. & ROWLEY, C.W. 2016 Characterizing and correcting for the effect of sensor noise in the dynamic mode decomposition. *Exp. Fluids* **57** (3), 42.
- DEWEY, P.A., CARRIOU, A. & SMITS, A.J. 2012 On the relationship between efficiency and wake structure of a batoid-inspired oscillating fin. *J. Fluid Mech.* **691**, 245–266.
- ELLINGTON, C.P., VAN DEN BERG, C., WILLMOTT, A.P. & THOMAS, A.L.R. 1996 Leading-edge vortices in insect flight. *Nature* **384** (6610), 626–630.
- ELOY, C. 2012 Optimal Strouhal number for swimming animals. *J. Fluids Struct.* **30**, 205–218.
- FLORYAN, D., VAN BUREN, T., ROWLEY, C.W. & SMITS, A.J. 2017 Scaling the propulsive performance of heaving and pitching foils. *J. Fluid Mech.* **822**, 386–397.
- FLORYAN, D., VAN BUREN, T. & SMITS, A.J. 2020 Swimmers' wake structures are not reliable indicators of swimming performance. *Bioinspir. Biomim.* **15** (2), 024001.
- HEMATI, M.S., ROWLEY, C.W., DEEM, E.A. & CATTAFESTA, L.N. 2017 De-biasing the dynamic mode decomposition for applied Koopman spectral analysis. *Theor. Comput. Fluid Dyn.* **31** (4), 349–368.
- HUSSAIN, A.K.M.F. & REYNOLDS, W.C. 1970 The mechanics of an organized wave in turbulent shear flow. *J. Fluid Mech.* **41** (2), 241–258.
- JONES, K., PLATZER, M., JONES, K. & PLATZER, M. 1997 Numerical computation of flapping-wing propulsion and power extraction. In *35th Aerospace Sciences Meeting and Exhibit, Reno, NV, USA*. AIAA.
- LENTINK, D., MUIJRES, F.T., DONKER-DUYVIS, F.J. & VAN LEEUWEN, J.L. 2008 Vortex-wake interactions of a flapping foil that models animal swimming and flight. *J. Expl Biol.* **211** (2), 267–273.
- LEWIN, G.C. & HAJ-HARIRI, H. 2003 Modelling thrust generation of a two-dimensional heaving airfoil in a viscous flow. *J. Fluid Mech.* **492**, 339–362.
- MACKOWSKI, A.W. & WILLIAMSON, C.H.K. 2015 Direct measurement of thrust and efficiency of an airfoil undergoing pure pitching. *J. Fluid Mech.* **765**, 524–543.
- MAGIONESI, F., DUBBIOSO, G., MUSCARI, R. & DI MASCIO, A. 2018 Modal analysis of the wake past a marine propeller. *J. Fluid Mech.* **855**, 469–502.
- MARESCA, C., FAVIER, D. & REBONT, J. 1979 Experiments on an aerofoil at high angle of incidence in longitudinal oscillations. *J. Fluid Mech.* **92** (4), 671–690.
- MCKINNEY, W. & DELAURIER, J. 1981 Wingmill: an oscillating-wing windmill. *J. Energy* **5** (2), 109–115.
- MOORED, K.W., DEWEY, P.A., BOSCHITSCH, B.M., SMITS, A.J. & HAJ-HARIRI, H. 2014 Linear instability mechanisms leading to optimally efficient locomotion with flexible propulsors. *Phys. Fluids* **26** (4), 041905.
- MOORED, K.W., DEWEY, P.A., SMITS, A.J. & HAJ-HARIRI, H. 2012 Hydrodynamic wake resonance as an underlying principle of efficient unsteady propulsion. *J. Fluid Mech.* **708**, 329–348.
- QUINN, D.B., LAUDER, G.V. & SMITS, A.J. 2015 Maximizing the efficiency of a flexible propulsor using experimental optimization. *J. Fluid Mech.* **767**, 430–448.
- RASPA, V., GODOY-DIANA, R. & THIRIA, B. 2013 Topology-induced effect in biomimetic propulsive wakes. *J. Fluid Mech.* **729**, 377–387.
- REYNOLDS, W.C. & HUSSAIN, A.K.M.F. 1972 The mechanics of an organized wave in turbulent shear flow. Part 3. Theoretical models and comparisons with experiments. *J. Fluid Mech.* **54** (2), 263–288.
- SARMAST, S., DADFAR, R., MIKKELSEN, R.F., SCHLATTER, P., IVANELL, S., SØRENSEN, J.N. & HENNINGSON, D.S. 2014 Mutual inductance instability of the tip vortices behind a wind turbine. *J. Fluid Mech.* **755**, 705–731.

*Connections between propulsive efficiency and wake structure*

- SCHMID, P.J. 2010 Dynamic mode decomposition of numerical and experimental data. *J. Fluid Mech.* **656**, 5–28.
- SCHNIPPER, T., ANDERSEN, A. & BOHR, T. 2009 Vortex wakes of a flapping foil. *J. Fluid Mech.* **633**, 411–423.
- SMITS, A.J. 2019 Undulatory and oscillatory swimming. *J. Fluid Mech.* **874**, P1.
- STROM, B., POLAGYE, B. & BRUNTON, S.L. 2022 Near-wake dynamics of a vertical-axis turbine. *J. Fluid Mech.* **935**, A6.
- TAIRA, K., HEMATI, M.S., BRUNTON, S.L., SUN, Y., DURAISAMY, K., BAGHERI, S., DAWSON, S.T.M. & YEH, C.-A. 2020 Modal analysis of fluid flows: applications and outlook. *AIAA J.* **58** (3), 998–1022.
- TAYLOR, G.K. 2018 Simple scaling law predicts peak efficiency in oscillatory propulsion. *Proc. Natl Acad. Sci. USA* **115** (32), 8063–8065.
- TAYLOR, J. 1997 *An Introduction to Error Analysis: The Study of Uncertainties in Physical Measurements*. University Science Books.
- TRIANTAFYLLOU, G.S., TRIANTAFYLLOU, M.S. & GROSENBAUGH, M.A. 1993 Optimal thrust development in oscillating foils with application to fish propulsion. *J. Fluids Struct.* **7** (2), 205–224.
- TU, J.H., ROWLEY, C.W., LUCHTENBURG, D.M., BRUNTON, S.L. & KUTZ, J.N. 2014 On dynamic mode decomposition: theory and applications. *J. Comput. Dyn.* **1** (2), 391–421.
- TYTELL, E.D. & LAUDER, G.V. 2004 The hydrodynamics of eel swimming. *J. Expl Biol.* **207** (11), 1825–1841.
- VAN BUREN, T., FLORYAN, D. & SMITS, A.J. 2020 *Bioinspired Underwater Propulsors*, pp. 113–139. Cambridge University Press.
- ZHANG, J. 2017 Footprints of a flapping wing. *J. Fluid Mech.* **818**, 1–4.